Nanoscale Advances

ROYAL SOCIETY OF CHEMISTRY

PAPER

View Article Online
View Journal | View Issue

Cite this: *Nanoscale Adv.*, 2025, **7**, 1962

The role of precursor coverage in the synthesis and substrate transfer of graphene nanoribbons†

Rimah Darawish,[ab] Oliver Braun,[cd] Klaus Müllen,[ef] Michel Calame,[cdg] Pascal Ruffieux,[a] Roman Fasel[ab] and Gabriela Borin Barin[*a]

Graphene nanoribbons (GNRs) with atomically precise widths and edge topologies have well-defined band gaps that depend on ribbon dimensions, making them ideal for room-temperature switching applications like field-effect transistors (FETs). For effective device integration, it is crucial to optimize growth conditions to maximize GNR length and, consequently, device yield. Equally important is establishing device integration and monitoring strategies that maintain GNR quality during the transition from growth to device fabrication. Here, we investigate the growth and alignment of 9-atom-wide armchair graphene nanoribbons (9-AGNRs) on a vicinal gold substrate, Au(788), with varying molecular precursor doses (PD) and, therefore, different resulting GNR coverages. Our investigation reveals that GNR growth location on Au(788) substrate is coverage-dependent. Scanning tunneling microscopy shows a strong correlation between GNR length evolution and both PD and GNR growth location. Employing Raman spectroscopy, samples with eight different PDs were analyzed. GNR alignment improves with length, achieving near-perfect alignment with an average length of ~40 nm for GNRs growing solely at the Au(788) step edges. To fully exploit GNR properties in device architectures, GNRs need to be transferred from their metallic growth substrate to semiconducting or insulating substrates. Upon transfer, samples with higher PD present systematically better alignment preservation and less surface disorder, attributed to reduced GNR mobility during the transfer process. Importantly, PD also affects the substrate transfer success rate, with higher success rates observed for samples with higher GNR coverages (77%) compared to lower GNR coverages (53%). Our findings characterize the important relationship between precursor dose, GNR length, alignment quality, and surface disorder during GNR growth and upon substrate transfer, offering crucial insights for the further development of GNR-based nanoelectronic devices.

Received 3rd January 2025
Accepted 3rd February 2025

DOI: 10.1039/d5na00017c

rsc.li/nanoscale-advances

Atomically precise graphene nanoribbons (GNRs) have gathered significant interest in recent years due to their tunable physicochemical properties,[1] achieved through precise control over their width[2] and edge structure.[2] This makes GNRs appealing candidates for various electronic,[3–7] spintronic,[8,9] and optical applications.[10–12]

Among the different types of GNRs, armchair-edged graphene nanoribbons (AGNRs) have attracted particular attention due to their width-dependent electronic band gap, which can be adjusted from quasi-metallic to wide band gap semiconductors.[13,14] AGNRs are classified into three families based on their width: $N = 3p$ (medium gap), $N = 3p + 1$ (wide gap), and $N = 3p + 2$ (quasi-metallic/narrow gap), where p is an integer and N indicates the number of carbon atoms along the GNR width. However, achieving a well-defined band gap requires precise control over the ribbons' width, edge structure, and length.

To synthesize atomically precise GNRs, on-surface synthesis is a versatile approach that involves assembling molecular building blocks on a catalyst substrate (usually Au(111)) under ultrahigh vacuum conditions.[15] This process is based on depositing suitably designed molecular precursors on the metal surface, followed by their surface-assisted covalent coupling. By carefully designing the precursor monomer, atomic precision over GNR width and edge topology is achieved, enabling the

[a]*Empa, Swiss Federal Laboratories for Materials Science and Technology, Nanotech@surfaces Laboratory, 8600 Dübendorf, Switzerland. E-mail: gabriela.borinbarin@empa.ch*

[b]*Department of Chemistry, Biochemistry and Pharmaceutical Sciences, University of Bern, 3012 Bern, Switzerland*

[c]*Empa, Swiss Federal Laboratories for Materials Science and Technology, Transport at Nanoscale Interfaces Laboratory, 8600 Dübendorf, Switzerland*

[d]*Department of Physics, University of Basel, 4056 Basel, Switzerland*

[e]*Max Planck Institute for Polymer Research, 55128 Mainz, Germany*

[f]*Department of Chemistry, Johannes Gutenberg University Mainz, Duesbergweg 10-14, 55128, Mainz, Germany*

[g]*Swiss Nanoscience Institute, University of Basel, 4056 Basel, Switzerland*

† Electronic supplementary information (ESI) available: Additional experimental data on: length evolution of 9-AGNRs on Au(788), average full-width at half maximum, peak positions, P, σ, and OD for 9-AGNRs on Au(788) and after transfer (ROS) across all PDs. A short discussion about the impact of inefficient transfer on GNR quality and alignment. See DOI: https://doi.org/10.1039/d5na00017c

synthesis of ultra-narrow GNRs with atomically precise widths (5-,[16] 7-,[15,17] 9-,[18] 13-[19] and 17-[20]AGNRs) and defined edge topology (armchair-, zigzag-,[21] chiral-,[22] and GNRs with topological phases[23,24]).

To fully exploit GNR properties in device architectures, GNRs need to be transferred from their metallic growth substrate to semiconducting or insulating substrates, such as SiO_2/Si. Various methods have been developed to transfer GNRs, depending on whether the growth substrate is a gold film or a single crystal. A polymer-free transfer is typically used for GNRs grown on Au(111) films on mica, using the gold film itself to support the GNRs throughout the transfer.[25] In the case of GNRs growing uniaxially aligned on a regularly stepped gold single crystal surface such as Au(788), the method of choice is an electrochemical delamination transfer.[11,26] This approach uses a polymer layer, usually poly(methyl methacrylate) (PMMA), to support the GNRs, and relies on water electrolysis to generate hydrogen bubbles at the interface between the PMMA/GNRs layer and the metal substrate. The hydrogen bubbles mechanically delaminate the PMMA/GNRs layer from the metal substrate, resulting in the transfer of uniaxially aligned GNRs.[11,26]

Among AGNRs, 9-atom-wide armchair GNRs (9-AGNRs) have been most extensively integrated into devices due to their suitable electronic gap (1.4 eV measured on Au)[18,27] enabling switching behavior at room temperature,[28] suitable length to bridge source and drain contacts[29] and mechanical robustness and chemical stability under ambient conditions.[25] Another important aspect of the integration of AGNRs into devices is the device yield, which typically ranges between 10–15% when using AGNRs grown on Au (111) surfaces, due to their non-preferential growth direction. By growing uniaxially aligned AGNRs, device yields can reach ~85%, as the GNRs can be deposited aligned with the source to drain direction of the device.[30]

Recent studies have further emphasized the importance of alignment and precursor design in achieving high-quality 9-AGNRs for device integration. Polarized Raman spectroscopy was used to quantitatively assess the alignment and quality of 9-AGNRs on different substrates, showing that very low-coverage samples grown on Au(788) achieve near-perfect uniaxial alignment, although alignment deteriorates after substrate transfer. On the other hand, samples with a full monolayer coverage retain alignment,[31] leading to higher yields when integrated into devices. Another study highlighted that using iodine-functionalized monomers significantly increases GNR lengths to 45 nm by separating the polymerization and cyclodehydrogenation steps.[29] This demonstrates how rational precursor design and reaction pathway optimization can maximize GNR properties for integration into nanoelectronic devices.

In this work, we investigate the growth of aligned 9-AGNRs on Au(788) and characterize their length as a function of precursor dose (PD) in 30 different samples using scanning tunneling microscopy (STM). We also characterize the quality of alignment and surface disorder as a function of PD (which inherently determines their length) on both the growth substrate (40 samples) and after substrate transfer (27 samples) using polarized Raman spectroscopy. Our results demonstrate that PD plays a key role in determining the quality of alignment and surface disorder, and significantly impacts the success rate of GNRs' substrate transfer.

Results and discussion

9-AGNR growth and length evolution on Au (788)

To investigate the growth of 9-AGNRs on a vicinal surface, we deposit the precursor molecule 3′,6′-di-iodine-1,1′:2′,1″-terphenyl (DITP)[29] onto Au(788) (kept at room temperature) at a fixed deposition rate of 1 Å min^{-1} (as measured with a quartz microbalance), with deposition times varying from 1 to 9 minutes. Subsequently, a 2-step thermal annealing process at 200 °C and 400 °C activate polymerization and induce cyclodehydrogenation, respectively, to form the final GNR structure.[18] By maintaining a constant deposition rate of 1 Å min^{-1} and increasing the deposition time in 1 minute steps, we achieve PDs ranging from 1 to 9 Å on the surface. Fig. 1a–h shows representative STM images of 9-AGNRs samples with PDs of 1 to 8–9 Å (where 8–9 Å corresponds to a full monolayer equivalency), respectively.

We observe that, as PD increases, the growth of 9-AGNRs on Au(788) occurs at three different positions. Initially, GNRs start growing along the Au(788) step edges, referred here as the 1st-row position (blue arrow). A representative STM image of 9-AGNRs with PD = 1 Å is presented in Fig. 1a, with short GNRs with an average length of 14 nm, growing solely at this position. As PD increases to 2 and 3 Å, GNRs continue to grow exclusively at the step edges with average GNR length reaching 19 nm and 35 nm, respectively (Fig. 1b and c). The growth of GNRs at the 1st-row position only, along the step edges, can be attributed to the higher catalytic activity and altered surface chemistry caused by the greater negative charge density at the lower step edge,[32,33] which facilitates the nucleation and growth process. For samples with low PD between 1 and 3 Å, the inter-ribbon distance remains constant and is determined by the width of the terraces, approximately 3.8 nm.[34]

For samples prepared with PD of 4 Å, the lower step edges are fully decorated with 9-AGNRs, and additional GNRs start to grow in the middle of the Au(788) terraces, referred here as the 2nd-row position (Fig. 1d, green arrow). Initially, GNRs at this position are also short, with an average length of 14 nm, due to the low amount of precursors available on the terraces. In some instances, such short GNRs also grow misaligned to the step edge (Fig. 1d, black arrow).

As PD further increases to 5 Å, 6 Å, and 7 Å, the average length of GNRs at the 2nd-row position steadily increases to 22 nm, 30 nm, and 36 nm, respectively (Fig. 1e–g). Notably, at PD = 7 Å, short GNRs (red arrow, Fig. 1g) also grow at the 3rd-row position close to the descending step edge of the terrace, with an average length of 13 nm. At PD = 8–9 Å, a complete monolayer is formed, with three rows of ribbons per terrace (Fig. 1h). In the monolayer samples, GNRs at the 1st-row exhibit an average length of 46 nm, the 2nd-row GNRs of 42 nm, and the 3rd-row GNRs of 36 nm. The insets in Fig. 1c, d and h show

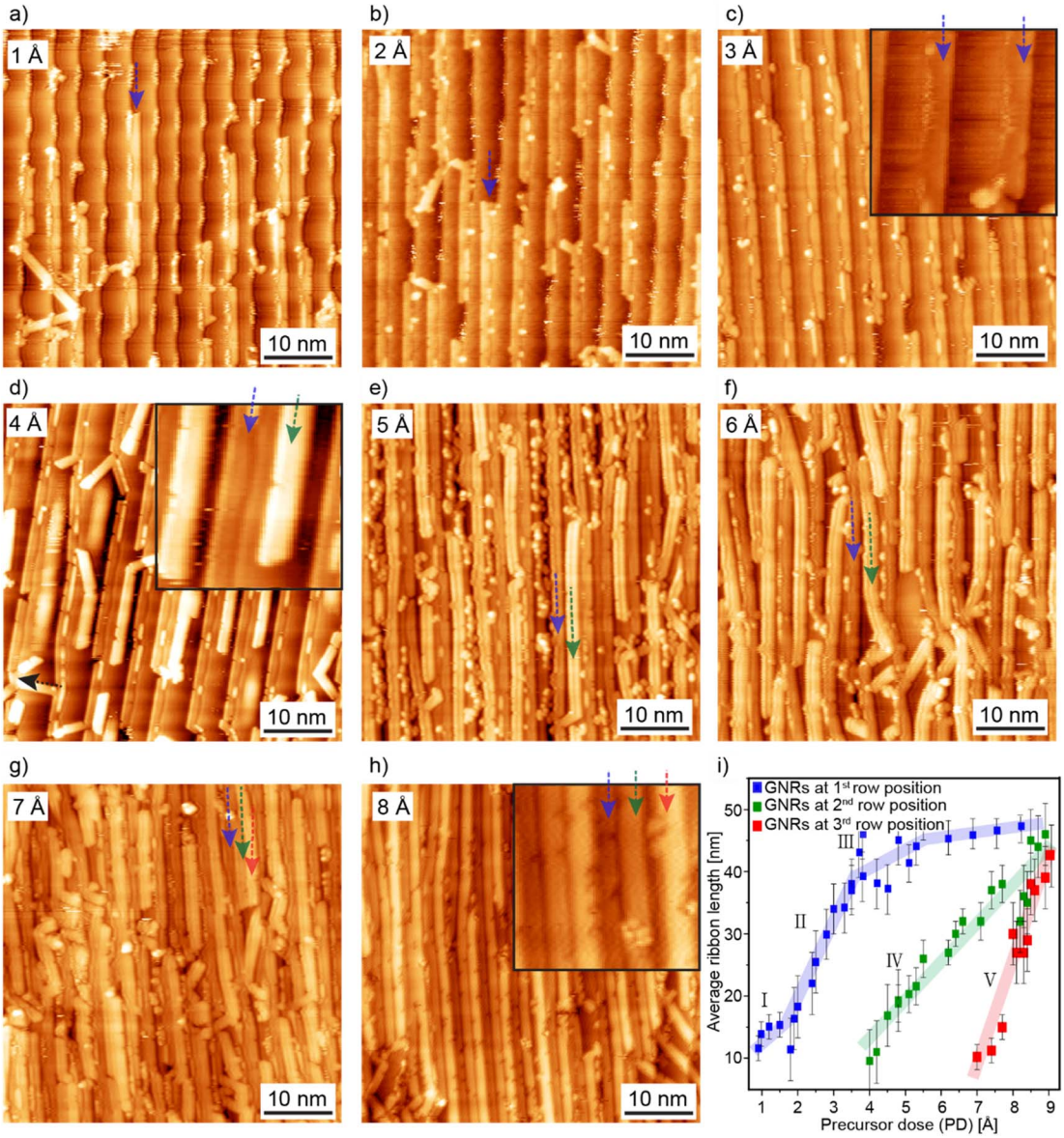

Fig. 1 Evolution of 9-AGNR growth on Au(788) with increasing precursor dose (PD). (a–c) STM images with GNR length evolution at the 1st-row position (blue arrows) along the lower step edges as PD increases from 1 to 3 Å. (d) STM image of GNRs at the 2nd-row position (green arrow) growing parallel to 1st-row GNRs (blue) at PD = 4 Å. (e–f) STM images revealing the length evolution of GNRs at the 2nd-row position (green arrows) at PD = 5 Å and PD = 6 Å, respectively. (g) STM image at PD = 7 Å, revealing the formation of a GNR at the 3rd-row position (red arrow), growing parallel to the GNRs grown previously at the 1st- and 2nd-row positions. (h) STM image of a monolayer of 9-AGNRs with GNRs grown in three parallel rows (blue, green, and red arrows) along each terrace at PD = 8 Å. (i) Histogram illustrating GNR length evolution for 30 samples across all PDs, with error bars representing standard deviation. Tunneling parameters for STM images: $V_b = -1.5$ V, $I_t = 30$ pA. Insets in (c), (d) and (h) are zoom-in of the same images for better visualization.

the presence of the most prominent defect in 9-AGNRs, known as bite defects. These defects occur due to the cleavage of phenyl groups in the precursor molecule during the cyclodehydrogenation step with density of 0.19 ± 0.10 nm^{-1} [18,35] and is independent of precursor dose.

Fig. 1i shows an overview of the length evolution of GNRs, displaying the average length distribution based on measurements of a total of 30 samples for PD ranging from 1 to 9 Å. Large-scale STM images (100 × 100 nm) were acquired, allowing for the examination of more than 800 GNRs per sample. As a complement, the average GNR lengths for selected PDs are summarized in Table S1.† The length evolution data displayed in Fig. 1i highlight the significantly different growth rates for GNRs growing at 1st-, 2nd-, and 3rd-row positions, as well as a non-linear growth behavior for 1st-row GNRs, which, however, can be approximated by a sequence of three linear regimes. We performed linear curve fitting to the data in Fig. 1i for each of the five regimes I to V of GNR length evolution, as discussed in the following.

Regime I corresponds to GNRs growing with PDs ranging from 0 to 2 Å. At these very low precursor coverages, GNR growth is dominated by nucleation at the step edges, more specifically at defect sites. This leads to a low growth rate of 5 nm $Å^{-1}$, and the average length of the nucleating GNRs thus only increases by 5 nm as PD increases from 1 to 2 Å. Upon increasing PD beyond 2 Å (regime II), the growth rate increases significantly to 16 nm $Å^{-1}$, with the average GNR length reaching 35 nm at PD = 3 Å. This corresponds to the situation where further GNR nucleation at the step edge is low, and most incoming precursors contribute to increasing the length of GNRs growing along the step edges. In regime III, starting at PD = 4 Å, all step edges become saturated, with only an incremental increase (4 nm $Å^{-1}$) in the average length of GNRs, up to the final average 1st-row GNR length of 43 nm. Before the step edges are fully passivated, GNRs also start to grow at the 2nd-row position (on the Au (788) terraces), here defined as regime IV (PD = 4 to 9 Å). In this regime a strictly linear length evolution occurs, leading to a steady increase in GNR length by 8 nm $Å^{-1}$. We attribute this relatively slow growth rate to a combination of significant nucleation density and the fact that, in this regime of 2nd-row GNR growth, incoming precursors also contribute to complete 1st-row GNRs and nucleation/lengthening of 3rd-row GNRs. Finally, when the 2nd-row GNR growth approaches saturation, GNRs start to grow a the 3rd-row position, close to the upper step edge of each terrace. This is regime V, with a high growth rate of 23 nm $Å^{-1}$, leading to a 3rd-row GNR length increase from 13 to 36 nm as PD increases from 7 to 9 Å. We attribute this rapid increase in GNR length to the presence of fewer nucleation sites, therefore the incoming precursors mostly contribute to the elongation of GNRs at this position.

As here, it appears that GNR growth at 1st-, 2nd, and 3rd-row positions is not a strictly sequential process, but Fig. 1i clearly shows that growth in the next row position starts before the previous row has been fully completed, as evidenced by the overlap of regimes III and IV as well as IV and V. This reflects the balance between nucleation and diffusion at play, which may be influenced by the growth temperature. We have not explored this aspect, which thus remains for future work. Overall, the detailed findings discussed above provide important insight into the growth of GNRs on vicinal surfaces and highlight the influence of growth position on the substrate and precursor dose on GNR length evolution.

9-AGNR quality and alignment as a function of PD on Au(788) and after substrate transfer

After transferring GNRs onto an insulating substrate, characterization using STM becomes infeasible due to the requirement for a conductive sample surface. Raman spectroscopy provides a non-destructive and rapid alternative for assessing GNR quality and orientation regardless of the substrate's nature.[11,26] Thus, a detailed Raman analysis for the samples studied above was performed.

The main Raman active mode for GNRs is the G mode, located in the high-frequency spectral range at ~1600 cm^{-1}.[36–38] This mode is present in all sp^2 carbon-based materials and originates from in-plane vibrations.[39] Additionally, several phonon modes are detected in the high-frequency spectral range of 1100–1500 cm^{-1}, which are associated with the edge structure of GNRs and collectively referred to as CH-D modes.[25,36–38] Specifically, the CH-bending mode at ~1200 cm^{-1} corresponds to the bending vibrations of the hydrogen atoms at the GNR edges, while the D mode at ~1300 cm^{-1} indicates disarrangement of the periodic graphene honeycomb lattice. It is important to note that unlike in graphene, the D peak in GNRs is an intrinsic mode resulting from the precise atomic edges,[25] rather than defects.[40] In the low-frequency range, two main intrinsic modes are present in GNRs: the radial breathing-like mode (RBLM) and the longitudinal compressive mode (LCM). The RBLM provides information about GNR width,[41,42] similar to the radial breathing mode (RBM) in carbon nanotubes (CNTs), with the frequency directly related to the diameter and chirality of the CNTs.[43] The LCM, on the other hand, is sensitive to GNR length, exhibiting a consistent frequency upshift for lengths below 10 nm.[44] In this present work we do not discuss the dependence of the LCM mode on sample coverage and length, as the average GNR length exceeds the threshold below which significant changes in this mode are typically observed.

Here, Raman measurements are conducted in a home-built vacuum chamber (~10^{-2} mbar) using 785 nm excitation wavelength (1.58 eV). In addition, an optimized mapping approach (maps of 10 μm × 10 μm, 10 × 10 pixels) is used to further limit damage to the GNRs.[26] Fig. 2a shows representative Raman spectra acquired directly on the growth substrate Au (788) for 9-AGNRs with PDs from 1 to 8 Å. In all spectra, the RBLM, CH, D, and G modes are observed, with the intensity of the Raman peaks increasing proportionally with PD. In samples with high PD, we observe an additional peak in the CH-D area at ~1302 cm^{-1} on Au(788). This additional peak may be related to the interaction between GNRs, likely due to the high coverage and shorter inter-GNR distances, however, further studies, such as temperature dependent Raman measurements, are needed to confirm the origin of this mode (Fig. 2a).

To investigate the electronic properties of GNRs in a device architecture, a substrate transfer process is required. Here, aligned 9-AGNRs are transferred from Au(788) onto a Raman-optimized substrate (ROS)[26] using electrochemical delamination transfer.[11,26] Fig. 2b depicts Raman spectra of 9-AGNRs with PD from 1–8 Å after substrate transfer onto a ROS. The presence of all 9-AGNR intrinsic Raman peaks (RBLM, CH, D, and G) after the substrate transfer process suggests the preservation of the GNRs' structural integrity during transfer. Additionally, the presence of additional modes are also observed, which we attribute to overtones, including the RBLM3 at 845 cm^{-1}.[26]

To evaluate GNR quality before and after substrate transfer, peak positions and the full-width at half maximum (FWHM) of RBLM, CH, D, and G modes are extracted for all samples. The results are summarized in Tables S2 and S3,† respectively. Upon substrate transfer, samples with medium and high PDs (4–8 Å) exhibit negligible changes in the FWHM for RBLM, D, CH, and G Raman modes, with all values falling within the experimental accuracy of the Raman measurements (3 cm^{-1}). However, low-

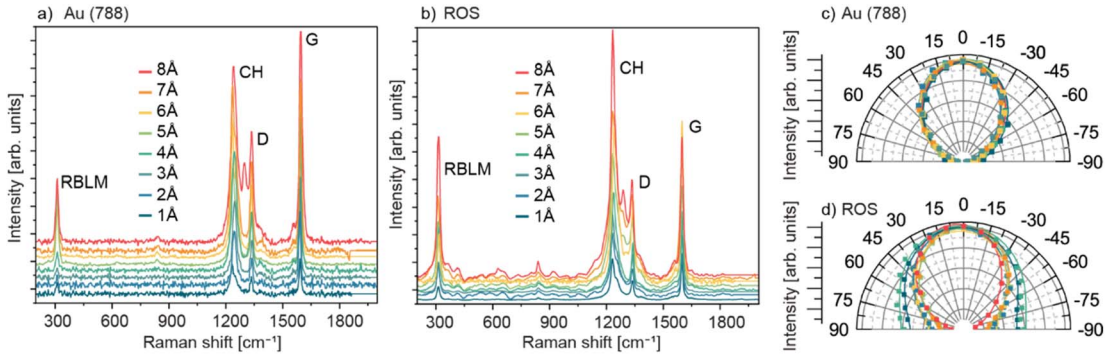

Fig. 2 Raman characterization of 9-AGNRs at PDs from 1–8 Å on Au(788) (a and c) and after substrate transfer onto ROS (b and d). Panels (c) and (d) polar plots of the polarization dependence of the G-mode for each PD on Au(788) and the ROS, respectively. The intensities in the polar plots are normalized to the 8 Å precursor dose. The incident light is polarized at an angle θ_{in} with respect to the orientation of the gold terraces (GNRs' alignment direction ($\theta = 0°$)), and the backscattered light is detected without an analyzing polarizer. The polar diagrams follow the $\cos^2(\theta)$ function as expected for this configuration and are fitted with a modified angular model based on ref. 31 (lines). The Raman measurements are obtained under vacuum conditions with a 785 nm excitation wavelength.

PD samples (1–3 Å), present a significant standard deviation in the FWHM between the samples in this range, particularly for the CH mode. The CH mode is an edge mode, and the increase in FWHM could be attributed to the presence of defects at the edges induced by the transfer process. This effect is particularly prominent in low PD samples where the only GNRs on the surface are attached to the step edges, which may exacerbate defects during the transfer.[31] Evaluation of the peak positions of the Raman active modes for all samples reveals negligible shifts in the G, D, and RBLM modes. However, the CH vibrational modes exhibit a notable downshift of 10–12 cm^{-1} across all PD samples which may be attributed to the different interaction of the edge modes with the ROS substrate compared to Au.

To achieve optimal performance in GNR-based FET devices and improve device yield, it is crucial to determine the alignment direction of GNRs such as to transfer them well aligned with the source to drain direction. Here we use polarized Raman spectroscopy to investigate the orientation of GNRs on the growth substrate and after substrate transfer. The laser excitation source (785 nm) is polarized from −90° to 90° at 10° increments, and the scattered light is detected without using an analyzing polarizer to maximize the overall signal.

By measuring the polarization-dependent intensity of scattered light, we observe that the Raman intensity of the G mode follows a $\cos^2(\theta_{in})$ polarization-dependent behavior, with maximum intensity at 0° and minimum at 90°, as shown in the polar plots in Fig. 2c and d. To quantitatively characterize the alignment of GNRs, two methods are employed. The first is the Raman polarization anisotropy (P),[11,31] defined by eqn (1):

$$P = (I_{\parallel} - I_{\perp})/(I_{\parallel} + I_{\perp}) \quad (1)$$

where $I_{\parallel}$ and $I_{\perp}$ represent the Raman intensities with polarization along and perpendicular to the GNR axis, respectively. A perfect uniaxial alignment of GNRs corresponds to $P = 1$, while $P = 0$ indicates random orientation. The second approach is an extended Gaussian distribution, initially detailed in our earlier work.[31] Here our previous model is modified, to take into account that no analyzing polarizer was used during the measurements, as in eqn (2).

$$I_{exp}(\vartheta) = A \times \int_{0°}^{360°} \cos^2(\varphi) \times \frac{1}{\sigma\sqrt{2\pi}} e^{-\frac{(\vartheta-\varphi-\vartheta_0)^2}{2\sigma^2}} d\varphi + B \times \frac{1}{2} \quad (2)$$

where ϑ_0 is the azimuthal angle along which GNRs are preferentially aligned; A is the fraction of surface area that exhibits aligned GNRs; σ is the width of the Gaussian distribution characterizing the angular distribution around ϑ_0 (quality of alignment); and B is the fraction of the surface area contributing to the isotropic, polarization-independent Raman signal. From A and B the overall disorder present on the surface is defined as: $OD = B/(B + A) \times 100\%$.[31]

Here, both methods are applied to investigate the alignment of GNRs for all PDs. To guarantee representative results 40 samples with PD ranging between 1–9 Å on the Au (788) and 27 samples after substrate transfer onto ROS are investigated. We extract P, σ, and OD for all Raman modes (RBLM, CH, D, and G), and summarize the results in Fig. 3 and Table 1 (for the G mode) and Fig. S1† (for the RBLM, CH, and D modes).

We start by discussing the low-PD regime, where GNRs grow solely on the step edges (highlighted in blue). In this regime, a clear trend is observed: $P_{Au(788)}$ increases and $\sigma_{Au(788)}$ becomes narrower as the length of GNRs increases, indicating a higher quality of alignment for longer GNRs on both Au(788) and ROS. GNRs grown at the 1st-row position with average lengths of 14, 19, and 35 nm (for PD = 1, 2, and 3 Å, respectively) have $P_{Au(788)}$ = 0.71, 0.82, and 0.90, and $\sigma_{Au(788)}$= 7°, 5°, and 3°, respectively (Fig. 3a, b and Table 1). These results are consistent with our STM studies (Fig. 1) and reflect that longer GNRs tend to better align with the step edge, while shorter GNRs can also grow across the gold terraces. At PD = 4 Å, where GNR growth at the 2nd-row position has started, we observe a kink in all curves of Fig. 3. The overall degree of GNR alignment decreases, with $P_{Au(788)} = 0.77$ and $\sigma_{Au(788)} = 6°$ (Fig. 3a and b). For this PD, the step edges are fully saturated, and GNRs grow at the 2nd-row position, located in the center of the terraces (highlighted in green), with an average length of 14 nm (Fig. 1d). As the 2nd-row

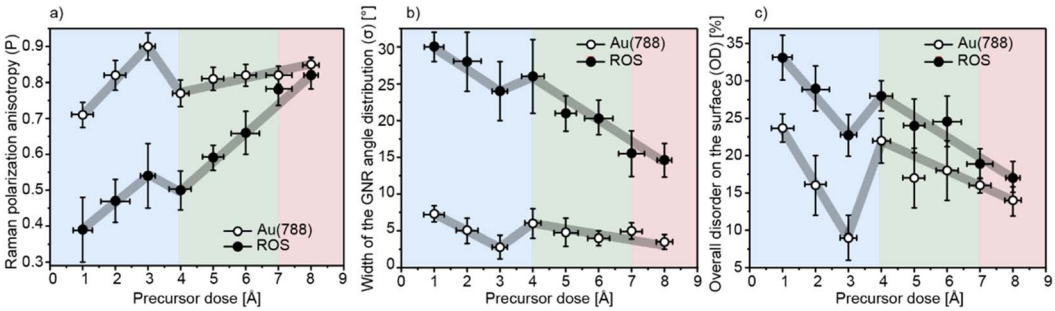

Fig. 3 Impact of PD on the alignment of GNRs on Au(788) and after substrate transfer onto ROS. Panels (a) polarization anisotropy (P), (b) width of GNR angle distribution (σ), and (c) overall disorder (OD) extracted for the G mode as a function of PD on both the Au(788) (open circles) and on ROS (closed circles) with error bars representing the standard deviation of the average values for each specific PD. The colored background represents the regimes in which GNRs grow preferentially at the 1st-row position (blue), at the 2nd-row position (green), and at the 3rd-row position (red) and the grey line is a guide to the eye.

GNRs grow longer, the quality of alignment improves again, reaching $P_{Au(788)} = 0.81$ and 0.82 with $\sigma_{Au(788)} = 5$ and 4° for precursor doses of 5 Å (average GNR length = 22 nm) and 6 Å (average GNR length = 30 nm), respectively. Finally, in the high-PD regime (highlighted in red), the substrate is fully covered with GNRs, and the quality of alignment reflects the behavior of GNRs grown at all three positions as a full monolayer: with $P_{Au(788)} = 0.82$ and 0.85, and $\sigma_{Au(788)} = 5°$ and 4° for PD = 7 Å and 8–9 Å, respectively (Fig. 3a and b). The appearance of GNRs at the 3rd-row position with an average length of 12 nm for PD = 7 Å does not negatively influence the quality of alignment, unlike the case of short GNRs grown with PD = 1 Å and 4 Å (Fig. 2c). At this particular PD, GNRs at the 3rd-row position grow well aligned because they are strictly confined between the 2nd-row GNRs and the upper step edge of the adjacent substrate terrace.

The evolution of P, σ, with PD for GNRs transferred onto the ROS follows the same trend, with overall increasing quality of alignment with increasing coverage, except for the same kink at PD = 4 Å. However, compared to GNRs on Au(788), substrate-transferred GNRs exhibit a significantly decreased P and an increased σ. In the low-PD regime (highlighted in blue), we extract $P_{ROS} = 0.39$, 0.47, and 0.55, and $\sigma_{ROS} =$ of 30°, 28°, and 24°, for PD = 1, 2, and 3 Å respectively. We attribute the striking reduction in alignment after substrate transfer to the strong interaction of GNRs with the Au(788) step edges, which hinders their transfer, along with increased GNR mobility due to the low coverage preparation (Fig. 3a and b and polar plots in Fig. 2d). For samples with PD = 4 Å, the degree of alignment decreases slightly, with $P_{ROS} = 0.5$ and $\sigma_{ROS} = 26°$, which we attribute to the presence of short GNRs growing at the 2nd-row position (Fig. 3a and b and polar plots in Fig. 2d). These short 2nd-row GNRs exhibit high mobility upon transfer, which negatively impacts their degree of alignment.

As PD increases, there is a steady increase in the preservation of alignment with $P_{ROS} = 0.65$, 0.7, 0.78, 0.82, and $\sigma_{ROS} = 21°$, 20°, 16°, and 15° for PD = 5 Å, 6 Å, 7 Å, and 8–9 Å, respectively. As the amount of GNRs on the surface increases (along with their length), their mobility during substrate transfer decreases, leading to a better preservation of alignment. Similar behavior was observed for full monolayer samples by Senkovskiy *et al.*,[11] Zhao *et al.*,[10] and by us in our previous work,[31] showing P = 0.72–0.82 after transfer. Overbeck *et al.*[44] also reported the influence of GNR length on polarization dependence for short 5-AGNRs with an average length of 3.8 nm, where the low polarization anisotropy ($P_{Au(788)}$ =0.3 before and $P_{ROS} = 0.4$ after substrate transfer) was attributed to GNRs' reduced shape anisotropy and the high mobility of short ribbons. These findings indicate that the observed trends in alignment preservation and polarization anisotropy in function of surface coverage (and length) may be generalized to other AGNRs, underscoring the broader applicability of our results.

Table 1 Average P, σ, and OD of the G mode as a function of PD, on Au(788) and ROS

Parameters	Raman polarization anisotropy (P)		Quality of alignment (σ) [°]		Overall disorder (OD) [%]	
Substrate	Au(788)	ROS	Au(788)	ROS	Au(788)	ROS
1 Å	0.71 ± 0.04	0.39 ± 0.09	7 ± 1	30 ± 2	24 ± 2	33 ± 3
2 Å	0.82 ± 0.04	0.47 ± 0.06	5 ± 2	28 ± 4	16 ± 4	29 ± 3
3 Å	0.90 ± 0.04	0.55 ± 0.09	3 ± 1	24 ± 4	9 ± 4	23 ± 3
4 Å	0.77 ± 0.02	0.50 ± 0.02	6 ± 2	26 ± 5	22 ± 3	28 ± 2
5 Å	0.81 ± 0.03	0.65 ± 0.04	5 ± 2	21 ± 1	17 ± 4	24 ± 4
6 Å	0.82 ± 0.03	0.70 ± 0.06	4 ± 1	20 ± 2	18 ± 4	25 ± 3
7 Å	0.82 ± 0.03	0.78 ± 0.02	5 ± 1	16 ± 4	16 ± 1	19 ± 2
8–9 Å	0.85 ± 0.02	0.82 ± 0.05	4 ± 1	15 ± 4	14 ± 3	17 ± 3

Next, we briefly discuss the overall disorder present on the surface (OD) for all samples before and after substrate transfer. The average values of OD for the G mode are presented in Fig. 3c and Table 1 (see Fig. S1† for RBLM, CH, and D modes). For samples on Au(788), the origin of $OD_{Au(788)}$ is attributed to very short GNRs, irregularly fused precursor monomers, and the presence of impurities from the precursor monomer. Here, there is a systematic decrease of $OD_{Au(788)}$ as the GNRs grow longer: $OD_{Au(788)} = 24\%$, 16%, and 9%, for samples with PD = 1, 2, and 3 Å, respectively (Fig. 3c, highlighted in blue). As GNRs start to grow at the 2nd-row position (PD = 4 Å, highlighted in green), $OD_{Au(788)}$ increases to 22%, which reflects the presence of very short GNRs (that do not exhibit polarization dependence) growing on the terraces. As PD continues to increase (and therefore GNR length), $OD_{Au(788)}$ linearly decreases, reaching 14% for the full monolayer. Upon substrate transfer, OD_{ROS} increases for all samples. However, the most significant increase is observed for low-PD samples, with $OD_{ROS} = 33\%$, 29%, and 23% (PD = 1, 2, and 3 Å, respectively), compared to the full monolayer $OD_{ROS} = 17\%$ (PD = 8–9 Å). This increase in OD likely arises from inefficient transfer in low-PD samples, resulting in partially broken GNRs, the presence of shorter GNRs with reduced shape anisotropy, and potentially contaminants introduced during the transfer process (such as PMMA).

Finally, we comment on the success rate of transferring GNR samples grown from different PDs. Initially, 40 samples of 9-AGNR on the Au(788) substrate were fabricated and studied, of which 27 samples were successfully transferred to the ROS. The transfer success rate, evaluated based on the quality of the Raman signal (Fig. S2†) is larger for samples with higher PD, 77% for PD = 7–9 Å, compared to those with medium PD = 4–6 Å (60%) and low PD = 1–3 Å (53%), endorsing our results that GNRs at higher coverages transfer more efficiently.

These findings not only enrich our understanding of the growth mechanism of GNRs on vicinal surfaces but also provide novel and crucial insights into the role of surface coverage in optimizing the transfer process, which is often the bottleneck for the device integration of high quality GNRs.

Conclusions

We investigated the growth and alignment of 9-AGNRs on Au(788) with varying precursor doses, both on the growth substrate and upon substrate transfer. We observed that GNRs grow sequentially at three positions on Au(788) depending on PD: only at the lower step edges at low precursor doses (and thus low coverages), in the middle of the terraces at medium doses, and at the upper step edges at coverages approaching a complete monolayer. In terms of alignment, longer GNRs show better unidirectional alignment on Au(788), achieving near-perfect alignment for PD = 3 Å, when a single row of GNRs saturates the Au(788) step edges. As PD increases and GNRs start to grow in the center of the terraces, the overall degree of alignment decreases due to the presence of short GNRs. A high degree of alignment is again obtained once a high PD is used to grow full monolayer samples. Upon substrate transfer, there is a significant decrease in the degree of alignment for low-PD samples, while alignment is largely preserved for high-PD ones. The overall disorder on the surface was also quantified. The presence of short GNRs increases the overall disorder on the growth surface, while a combination of short GNRs and impurities increases the overall disorder after substrate transfer. Finally, we also find a PD-dependent substrate transfer success rate, with samples grown from higher PD being more successfully transferred (77%) than lower PD samples (53%). Our work unravels the role of precursor dose on the growth of 9-AGNRs, their length evolution, quality of alignment, and overall surface disorder. By systematically examining these parameters across varying coverages (and several samples per coverage) we hope to improve the understanding of how surface coverage influences the properties of the GNRs once transferred into a device. We believe this study will support a better understanding of GNR samples integrated into devices leading to the optimization of single and multi-GNR devices.

Methods

On-surface synthesis and STM characterization of 9-AGNRs

Au(788) single crystal growth substrate (MaTecK GmbH, Germany) was cleaned in ultra-high vacuum (UHV) with two cycles of sputtering at 1 kV Ar+ (for 10 minutes) and annealing at 420 °C (for 10 minutes). Subsequently, the 9-AGNR precursor monomer, 3′,6′-di-iodine-1,1′:2′,1″-terphenyl (DITP),[29] was sublimated onto the pristine Au surface from a quartz crucible heated to 70 °C, while the substrate remained at room temperature. To control the deposition rate, a quartz microbalance was employed to maintain a constant deposition rate of 1 Å min^{-1}. This deposition rate is not calibrated to accurately correspond to the true surface coverage. Instead, it is calibrated relative to a standard measurement obtained through STM, by counting the number of GNRs. 8–9 Å corresponds to the amount of precursor molecules resulting in GNR monolayer saturation coverage. Following deposition, with deposition times varying to afford from 1 to 9 Å deposits, the substrate was heated to 200 °C (0.5 K s^{-1}) for 10 minutes to initiate DITP polymerization, followed by annealing at 400 °C (0.5 K s^{-1}) for 10 minutes to induce cyclodehydrogenation. After the sample cooled down to room temperature (RT), STM images were acquired at RT in constant current mode, typically with a −1.5 V sample bias and a 0.03 nA setpoint current using a Scienta Omicron VT-STM.

Transfer of GNRs to ROS

To transfer the 9-AGNRs from the Au(788) growth substrate to ROS, electrochemical delamination was used. First, a support layer of poly(methyl methacrylate) (PMMA) was spin-coated (4 PMMA layers, 2500 rpm for 90 s) on the 9-AGNR/Au(788) surface, followed by a 10 minutes curing process at 80 °C. PMMA was removed from the Au(788) crystal's edges using a two-step process: 80 minutes UV exposure (leading to the breakdown of the chemical bonds in the PMMA), followed by a 3 minutes development in water/isopropanol (to remove the PMMA from the surface's edges). Electrochemical delamination was performed in an aqueous solution of NaOH (1 M) as the

electrolyte. A DC voltage of 5 V (current ~0.2 A) was applied between the PMMA/9-AGNR/Au(788) cathode and a glassy carbon electrode used as the anode. At the interface between PMMA/GNRs and Au, hydrogen bubbles form, resulting from the water reduction: $2H_2O(l) + 2e^- \rightarrow H_2(g) + 2OH^-(aq)$. The H_2 bubbles mechanically delaminate the PMMA/GNR layer from the Au(788) surface. The delaminated PMMA/GNR layer was left in ultra-pure water for 5 minutes before being transferred to the target substrate. The delaminated PMMA/GNR layer was transferred to the ROS followed by a two-step annealing: 80 °C for 10 minutes + 110 °C for 20 minutes to improve adhesion between the ROS and the PMMA/GNR layer. Finally, PMMA was dissolved in acetone for 15 minutes, and the resulting GNR/ROS was rinsed with ethanol and ultra-pure water.

Raman spectroscopy

Raman spectroscopy measurements were performed using a WITec confocal Raman microscope (WITec Alpha 300R) with a 785 nm (1.5 eV) laser line and a power of 40 mW. A 50× microscope objective was used to focus the laser beam on the sample and collect the scattered light. The Raman spectra were calibrated using the Si peak at 520.5 cm^{-1}. The laser wavelength, power, and integration time were optimized for each substrate to maximize the signal while minimizing sample damage. To prevent sample damage, a Raman mapping approach with a size of 10 × 10 pixels (10 × 10 μm) was employed, and the measurements were conducted in a home-built vacuum chamber at a pressure of approximately 10^{-2} mbar. Polarized Raman measurements were conducted without the analyzing polarizer to collect all the scattered light. A motorized half-wave plate was used to change the polarization direction of the incident laser beam from −90° to +90° in steps of 10°. The scattered signal, with an excitation wavelength of 785 nm, was detected with a 300 mm lens-based spectrometer equipped with a grating of 300 g mm^{-1} (grooves per mm) and a cooled deep-depletion CCD.

Using the WITec software, a cosmic ray filter was applied to all raw maps to remove signatures of photoluminescence. Afterward, the Raman maps were averaged and polynomial background subtraction was applied, followed by batched fitting with a Lorentzian function for all polarization angles between −90° to 90° for each Raman mode. The fitting using the equations mentioned in the results and discussion was done in IGOR Pro software (Wavemetrics Inc.), and the fitting parameters were obtained through the lowest stable Chi-square values.

Data availability

All raw data will be made available by the authors on reasonable request.

Conflicts of interest

There are no conflicts to declare.

Acknowledgements

This work was supported by the Swiss National Science Foundation under grant no. 200020_182015, the European Union Horizon 2020 research and innovation program under grant agreement no. 881603 (GrapheneFlagship Core 3) the European Union Horizon 2020 FET Open project no. 767187 (QuIET), the Office of Naval Research BRC Program under the grant N00014-18-1-2708 and the European Innovation Council Pathfinder project no. 101099098 (ATYPIQUAL). The authors also greatly appreciate the financial support from the Werner Siemens Foundation (CarboQuant). R.D. acknowledges funding from the University of Bern. For the purpose of Open Access, the author has applied a CC BY public copyright license to any Author Accepted Manuscript version arising from this submission.

References

1 C. Tian, W. Miao, L. Zhao and J. Wang, Graphene Nanoribbons: Current Status and Challenges as Quasi-One-Dimensional Nanomaterials, *Rev. Phys*, 2023, **10**, 100082, DOI: 10.1016/j.revip.2023.100082.

2 R. S. K. Houtsma, J. Rie and M. Stöhr, Atomically Precise Graphene Nanoribbons: Interplay of Structural and Electronic Properties, *Chem. Soc. Rev.*, 2021, **50**(11), 6541–6568, DOI: 10.1039/D0CS01541E.

3 P. B. Bennett, Z. Pedramrazi, A. Madani, Y.-C. Chen, D. G. de Oteyza, C. Chen, F. R. Fischer, M. F. Crommie and J. Bokor, Bottom-up Graphene Nanoribbon Field-Effect Transistors, *Appl. Phys. Lett.*, 2013, **103**(25), 253114, DOI: 10.1063/1.4855116.

4 Z. Mutlu; Y. Lin; G. B. Barin; Z. Zhang; G. Pitner; S. Wang; R. Darawish; M. D. Giovannantonio; H. Wang; J. Cai; M. Passlack; C. H. Diaz; A. Narita; K. Müllen; F. R. Fischer; P. Bandaru; A. C. Kummel; P. Ruffieux; R. Fasel and J. Bokor Short-Channel Double-Gate FETs with Atomically Precise Graphene Nanoribbons. In *2021 IEEE International Electron Devices Meeting (IEDM)*; 2021; pp. 37.4.1–37.4.4. doi: DOI: 10.1109/IEDM19574.2021.9720620.

5 J. Zhang, L. Qian, G. B. Barin, A. H. S. Daaoub, P. Chen, K. Müllen, S. Sangtarash, P. Ruffieux, R. Fasel, H. Sadeghi, J. Zhang, M. Calame and M. L. Perrin, Contacting Individual Graphene Nanoribbons Using Carbon Nanotube Electrodes, *Nat Electron*, 2023, **6**(8), 572–581, DOI: 10.1038/s41928-023-00991-3.

6 Z. Chen, A. Narita and K. Müllen, Graphene Nanoribbons: On-Surface Synthesis and Integration into Electronic Devices, *Adv. Mater.*, 2020, **32**, 2001893, DOI: 10.1002/adma.202001893.

7 V. Passi, A. Gahoi, B. V. Senkovskiy, D. Haberer, F. R. Fischer, A. Grüneis and M. C. Lemme, Field-Effect Transistors Based on Networks of Highly Aligned, Chemically Synthesized $N = 7$ Armchair Graphene Nanoribbons, *ACS Appl. Mater. Nat. Electron*, 2018, **10**(12), 9900–9903, DOI: 10.1021/acsami.8b01116.

8 M. Slota, A. Keerthi, W. K. Myers, E. Tretyakov, M. Baumgarten, A. Ardavan, H. Sadeghi, C. J. Lambert,

A. Narita, K. Müllen and L. Bogani, Magnetic Edge States and Coherent Manipulation of Graphene Nanoribbons, *Nature*, 2018, **557**(7707), 691–695, DOI: 10.1038/s41586-018-0154-7.

9 H. Wang, H. S. Wang, C. Ma, L. Chen, C. Jiang, C. Chen, X. Xie, A.-P. Li and X. Wang, Graphene Nanoribbons for Quantum Electronics, *Nat. Rev. Phys.*, 2021, **3**(12), 791–802, DOI: 10.1038/s42254-021-00370-x.

10 S. Zhao, G. B. Barin, T. Cao, J. Overbeck, R. Darawish, T. Lyu, S. Drapcho, S. Wang, T. Dumslaff, A. Narita, M. Calame, K. Müllen, S. G. Louie, P. Ruffieux, R. Fasel and F. Wang, Optical Imaging and Spectroscopy of Atomically Precise Armchair Graphene Nanoribbons, *Nano Lett.*, 2020, **20**(2), 1124–1130, DOI: 10.1021/acs.nanolett.9b04497.

11 B. V. Senkovskiy, M. Pfeiffer, S. K. Alavi, A. Bliesener, J. Zhu, S. Michel, A. V. Fedorov, R. German, D. Hertel, D. Haberer, L. Petaccia, F. R. Fischer, K. Meerholz, P. H. M. van Loosdrecht, K. Lindfors and A. Grüneis, Making Graphene Nanoribbons Photoluminescent, *Nano Lett.*, 2017, **17**(7), 4029–4037, DOI: 10.1021/acs.nanolett.7b00147.

12 S. Jiang, T. Neuman, A. Boeglin, F. Scheurer and G. Schull, Topologically Localized Excitons in Single Graphene Nanoribbons, *Science*, 2023, **379**(6636), 1049–1054, DOI: 10.1126/science.abq6948.

13 L. Yang, C.-H. Park, Y.-W. Son, M. L. Cohen and S. G. Louie, Quasiparticle Energies and Band Gaps in Graphene Nanoribbons, *Phys. Rev. Lett.*, 2007, **99**(18), 186801, DOI: 10.1103/PhysRevLett.99.186801.

14 M. Corso; E. Carbonell-Sanromà and D. G. de. Oteyza Bottom-Up Fabrication of Atomically Precise Graphene Nanoribbons. In *On-Surface Synthesis II; Advances in Atom and Single Molecule Machines*; Springer, Cham, 2018; pp. 113–152. doi: DOI: 10.1007/978-3-319-75810-7_6.

15 J. Cai, P. Ruffieux, R. Jaafar, M. Bieri, T. Braun, S. Blankenburg, M. Muoth, A. P. Seitsonen, M. Saleh, X. Feng, K. Müllen and R. Fasel, Atomically Precise Bottom-up Fabrication of Graphene Nanoribbons, *Nature*, 2010, **466**(7305), 470–473, DOI: 10.1038/nature09211.

16 A. Kimouche, M. M. Ervasti, R. Drost, S. Halonen, A. Harju, P. M. Joensuu, J. Sainio and P. Liljeroth, Ultra-Narrow Metallic Armchair Graphene Nanoribbons, *Nat. Commun.*, 2015, **6**, 10177, DOI: 10.1038/ncomms10177.

17 A. Ishii, A. Shiotari and Y. Sugimoto, Quality Control of On-Surface-Synthesised Seven-Atom Wide Armchair Graphene Nanoribbons, *Nanoscale*, 2020, **12**(12), 6651–6657, DOI: 10.1039/C9NR10942K.

18 L. Talirz, H. Söde, T. Dumslaff, S. Wang, J. R. Sanchez-Valencia, J. Liu, P. Shinde, C. A. Pignedoli, L. Liang, V. Meunier, N. C. Plumb, M. Shi, X. Feng, A. Narita, K. Müllen, R. Fasel and P. Ruffieux, On-Surface Synthesis and Characterization of 9-Atom Wide Armchair Graphene Nanoribbons, *ACS Nano*, 2017, **11**(2), 1380–1388, DOI: 10.1021/acsnano.6b06405.

19 Y.-C. Chen, D. G. de Oteyza, Z. Pedramrazi, C. Chen, F. R. Fischer and M. F. Crommie, Tuning the Band Gap of Graphene Nanoribbons Synthesized from Molecular Precursors, *ACS Nano*, 2013, 7(7), 6123–6128, DOI: 10.1021/nn401948e.

20 J. Yamaguchi, H. Hayashi, H. Jippo, A. Shiotari, M. Ohtomo, M. Sakakura, N. Hieda, N. Aratani, M. Ohfuchi, Y. Sugimoto, H. Yamada and S. Sato, Small Bandgap in Atomically Precise 17-Atom-Wide Armchair-Edged Graphene Nanoribbons, *Commun. Mater.*, 2020, **1**(1), 1–9, DOI: 10.1038/s43246-020-0039-9.

21 P. Ruffieux, S. Wang, B. Yang, C. Sánchez-Sánchez, J. Liu, T. Dienel, L. Talirz, P. Shinde, C. A. Pignedoli, D. Passerone, T. Dumslaff, X. Feng, K. Müllen and R. Fasel, On-Surface Synthesis of Graphene Nanoribbons with Zigzag Edge Topology, *Nature*, 2016, **531**(7595), 489–492, DOI: 10.1038/nature17151.

22 D. G. Oteyza, A. García-Lekue, M. Vilas-Varela, N. Merino-Díez, E. Carbonell-Sanromà, M. Corso, G. Vasseur, C. Rogero, E. Guitián, J. I. Pascual, J. E. Ortega, Y. Wakayama and D. Peña, Substrate-Independent Growth of Atomically Precise Chiral Graphene Nanoribbons, *ACS Nano*, 2016, **10**(9), 9000–9008, DOI: 10.1021/acsnano.6b05269.

23 O. Gröning, S. Wang, X. Yao, C. A. Pignedoli, G. Borin Barin, C. Daniels, A. Cupo, V. Meunier, X. Feng, A. Narita, K. Müllen, P. Ruffieux and R. Fasel, Engineering of Robust Topological Quantum Phases in Graphene Nanoribbons, *Nature*, 2018, **560**(7717), 209–213, DOI: 10.1038/s41586-018-0375-9.

24 D. J. Rizzo, G. Veber, T. Cao, C. Bronner, T. Chen, F. Zhao, H. Rodriguez, S. G. Louie, M. F. Crommie and F. R. Fischer, Topological Band Engineering of Graphene Nanoribbons, *Nature*, 2018, **560**(7717), 204–208, DOI: 10.1038/s41586-018-0376-8.

25 G. B. Barin, A. Fairbrother, L. Rotach, M. Bayle, M. Paillet, L. Liang, V. Meunier, R. Hauert, T. Dumslaff, A. Narita, K. Müllen, H. Sahabudeen, R. Berger, X. Feng, R. Fasel and P. Ruffieux, Surface-Synthesized Graphene Nanoribbons for Room-Temperature Switching Devices: Substrate Transfer and Ex-Situ Characterization, *ACS Appl. Nano Mater.*, 2019, **2**(4), 2184–2192, DOI: 10.1021/acsanm.9b00151.

26 J. Overbeck, G. Borin Barin, C. Daniels, M. L. Perrin, L. Liang, O. Braun, R. Darawish, B. Burkhardt, T. Dumslaff, X.-Y. Wang, A. Narita, K. Müllen, V. Meunier, R. Fasel, M. Calame and P. Ruffieux, Optimized Substrates and Measurement Approaches for Raman Spectroscopy of Graphene Nanoribbons, *Phys. Status Solidi B*, 2019, **256**(12), 1900343, DOI: 10.1002/pssb.201900343.

27 B. V. Senkovskiy, D. Haberer, D. Yu. Usachov, A. V. Fedorov, N. Ehlen, M. Hell, L. Petaccia, G. Di Santo, R. A. Durr, F. R. Fischer and A. Grüneis, Spectroscopic Characterization of $N = 9$ Armchair Graphene Nanoribbons: Spectroscopic Characterization of $N = 9$ Armchair Graphene Nanoribbons, *Phys. Status Solidi RRL*, 2017, **11**(8), 1700157, DOI: 10.1002/pssr.201700157.

28 J. P. Llinas, A. Fairbrother, G. Borin Barin, W. Shi, K. Lee, S. Wu, B. Yong Choi, R. Braganza, J. Lear, N. Kau, W. Choi, C. Chen, Z. Pedramrazi, T. Dumslaff, A. Narita, X. Feng, K. Müllen, F. Fischer, A. Zettl, P. Ruffieux, E. Yablonovitch, M. Crommie, R. Fasel and J. Bokor, Short-Channel Field-Effect Transistors with 9-Atom and 13-Atom Wide

Graphene Nanoribbons, *Nat. Commun.*, 2017, **8**(1), 633, DOI: 10.1038/s41467-017-00734-x.

29 M. Di Giovannantonio, O. Deniz, J. I. Urgel, R. Widmer, T. Dienel, S. Stolz, C. Sánchez-Sánchez, M. Muntwiler, T. Dumslaff, R. Berger, A. Narita, X. Feng, K. Müllen, P. Ruffieux and R. Fasel, On-Surface Growth Dynamics of Graphene Nanoribbons: The Role of Halogen Functionalization, *ACS Nano*, 2018, **12**(1), 74–81, DOI: 10.1021/acsnano.7b07077.

30 G. Borin Barin, Q. Sun, M. Di Giovannantonio, C. Du, X. Wang, J. P. Llinas, Z. Mutlu, Y. Lin, J. Wilhelm, J. Overbeck, C. Daniels, M. Lamparski, H. Sahabudeen, M. L. Perrin, J. I. Urgel, S. Mishra, A. Kinikar, R. Widmer, S. Stolz, M. Bommert, C. Pignedoli, X. Feng, M. Calame, K. Müllen, A. Narita, V. Meunier, J. Bokor, R. Fasel and P. Ruffieux, Growth Optimization and Device Integration of Narrow-Bandgap Graphene Nanoribbons, *Small*, 2022, **18**, 2202301, DOI: 10.1002/smll.202202301.

31 R. Darawish, J. Overbeck, K. Müllen, M. Calame, P. Ruffieux, R. Fasel and G. Borin Barin, Quantifying Alignment and Quality of Graphene Nanoribbons: A Polarized Raman Spectroscopy Approach, *Carbon*, 2024, **218**, 118688, DOI: 10.1016/j.carbon.2023.118688.

32 T. Classen, G. Fratesi, G. Costantini, S. Fabris, F. L. Stadler, C. Kim, S. de Gironcoli, S. Baroni and K. Kern, Templated Growth of Metal-Organic Coordination Chains at Surfaces, *Angew. Chem., Int. Ed.*, 2005, **44**(38), 6142–6145, DOI: 10.1002/anie.200502007.

33 M. E. Cañas-Ventura, W. Xiao, D. Wasserfallen, K. Müllen, H. Brune, J. V. Barth and R. Fasel, Self-Assembly of Periodic Bicomponent Wires and Ribbons, *Angew. Chem., Int. Ed.*, 2007, **46**(11), 1814–1818, DOI: 10.1002/anie.200604083.

34 S. Rousset, V. Repain, G. Baudot, Y. Garreau and J. Lecoeur, Self-Ordering of Au(111) Vicinal Surfaces and Application to Nanostructure Organized Growth, *J. Phys.: Condens. Matter*, 2003, **15**(47), S3363–S3392, DOI: 10.1088/0953-8984/15/47/009.

35 M. Pizzochero, K. Čerņevičs, G. Borin Barin, S. Wang, P. Ruffieux, R. Fasel and O. V. Yazyev, Quantum Electronic Transport Across "Bite" Defects in Graphene Nanoribbons, *2D Mater.*, 2021, **8**, 035025, DOI: 10.1088/2053-1583/abf716.

36 R. Gillen, M. Mohr, C. Thomsen and J. Maultzsch, Vibrational Properties of Graphene Nanoribbons by First-Principles Calculations, *Phys. Rev. B*, 2009, **80**(15), 155418, DOI: 10.1103/PhysRevB.80.155418.

37 R. Gillen, M. Mohr and J. Maultzsch, Symmetry Properties of Vibrational Modes in Graphene Nanoribbons, *Phys. Rev. B*, 2010, **81**(20), 205426, DOI: 10.1103/PhysRevB.81.205426.

38 I. A. Verzhbitskiy, M. D. Corato, A. Ruini, E. Molinari, A. Narita, Y. Hu, M. G. Schwab, M. Bruna, D. Yoon, S. Milana, X. Feng, K. Müllen, A. C. Ferrari, C. Casiraghi and D. Prezzi, Raman Fingerprints of Atomically Precise Graphene Nanoribbons, *Nano Lett.*, 2016, **16**(6), 3442–3447, DOI: 10.1021/acs.nanolett.5b04183.

39 A. Maghsoumi, L. Brambilla, C. Castiglioni, K. Müllen and M. Tommasini, Overtone and Combination Features of G and D Peaks in Resonance Raman Spectroscopy of the C78H26 Polycyclic Aromatic Hydrocarbon, *J. Raman Spectrosc.*, 2015, **46**(9), 757–764, DOI: 10.1002/jrs.4717.

40 A. Eckmann, A. Felten, I. Verzhbitskiy, R. Davey and C. Casiraghi, Raman Study on Defective Graphene: Effect of the Excitation Energy, Type, and Amount of Defects, *Phys. Rev. B*, 2013, **88**(3), 035426, DOI: 10.1103/PhysRevB.88.035426.

41 D. Liu, C. Daniels, V. Meunier, A. G. Every and D. Tománek, In-Plane Breathing and Shear Modes in Low-Dimensional Nanostructures, *Carbon*, 2020, **157**, 364–370, DOI: 10.1016/j.carbon.2019.10.041.

42 J. Zhou and J. Dong, Vibrational Property and Raman Spectrum of Carbon Nanoribbon, *Appl. Phys. Lett.*, 2007, **91**(17), 173108, DOI: 10.1063/1.2800796.

43 D. I. Levshov, H. N. Tran, M. Paillet, R. Arenal, X. T. Than, A. A. Zahab, Y. I. Yuzyuk, J.-L. Sauvajol and T. Michel, Accurate Determination of the Chiral Indices of Individual Carbon Nanotubes by Combining Electron Diffraction and Resonant Raman Spectroscopy, *Carbon*, 2017, **114**, 141–159, DOI: 10.1016/j.carbon.2016.11.076.

44 J. Overbeck, G. B. Barin, C. Daniels, M. L. Perrin, O. Braun, Q. Sun, R. Darawish, M. De Luca, X.-Y. Wang, T. Dumslaff, A. Narita, K. Müllen, P. Ruffieux, V. Meunier, R. Fasel and M. Calame, A Universal Length-Dependent Vibrational Mode in Graphene Nanoribbons, *ACS Nano*, 2019, **13**(11), 13083–13091, DOI: 10.1021/acsnano.9b05817.